Aerodynamic Performance Prediction of a Wind Turbine in Steady and Unsteady Conditions Using a Panel Method

Leonardo Buralli
leonardoburalli1995@gmail.com

Instituto Superior Técnico, Universidade de Lisboa, Portugal

July 2021

Abstract

In the recent years the wind industry has seen one of fastest-growing technological development in the energy sector, playing a massive role in the energy transition. Wind turbines operate in a very unsteady environment, therefore experiencing variable effects (i.e. sudden change in wind speed). This can result in large oscillations of the loads on the turbine blades and tower, consequently affecting the performance of such systems. The purpose of this work is the aerodynamic study under steady and unsteady inflow conditions of a wind turbine designed for the New MEXICO experiment using the three-dimensional panel method developed at Instituto Superior Técnico (IST), *PROPAN*. First, an extensive numerical study under steady inflow conditions is performed to obtain a well-defined turbine grid to be utilised as input for the dynamic simulations. Two undisturbed wind velocities, 10.05 m/s ($TSR = 10$) and 15.06 m/s ($TSR = 6.7$), are considered. When comparing the simulated results with the New MEXICO experimental data, a good agreement is generally found. Second, the dynamic blade pitch variation and its effect on the blade loads at $TSR = 10$ are described. Two different methods to create the wake geometry were applied, with the main difference of yielding a wake geometry either partially or fully aligned to the incoming wind flow. The forces predicted with both wake geometries are comparable to the experimental ones when achieving the steady state solution. On the other hand, the force undershoot and overshoot occurring after the pitch modification can not be captured properly.
Keywords: Wind Turbine, Panel Method, Dynamic Inflow, MEXICO.

1. Introduction

The implementation of energy systems running on renewable sources, together with the introduction of strong and courageous governmental energy policies, is fundamental to tackle climate change and achieve the global emissions reduction goals signed in the Paris Agreement. Wind industry has seen one of fastest-growing technological development in the energy sector, passing from an average of 1 MW turbines installed at the beginning of this century to the recent production of turbines with a rated capacity up to 15 MW.

Aerodynamic load is part of the decisive effects that wind turbine must consider. It directly affects the structural design of a wind turbine blade, the design of the generator set and the design of control system [1]. Therefore, performance forecasting is fundamental when designing a wind turbine and its accuracy plays a central role in the economic feasibility of wind farm projects. Since wind turbine operate in a very unsteady environment, dynamic inflow has a large importance. This phenomenon happens when a sudden change in pitch angle, rotor speed or wind speed occurs. Because of this, the wake behind the turbine, and consequently the induction and the resulting effective velocity in the rotor plane will achieve steady state conditions only after a certain delay. The effects of this behaviour in the wake have a large practical importance, not only in view of the higher dynamic loads experienced by the turbine but also because of its impact on the aerodynamic damping characteristics and in particular in the design of pitch control algorithms [2].

Most of the present wind turbine design codes are based on Blade Element Momentum (BEM) theory which can be considered as a combination of the Blade Element Theory and the Momentum Theory [3]. Beside its simplicity, BEM is derived from stationary conditions while wind turbines operate at a very unsteady environment. A more sophisticated but still computationally efficient approach to account for the complex flow phenomena on wind turbine rotors can be found in the lifting-line (LL) theory [4]. This method offers several advantages over BEM, such as a more accurate relationship be-

tween the induction velocities and the radial circulation distribution. On the other hand, it relies on the unrealistic assumption of having a rigid wake, limiting its accuracy when compared to experimental data [5]. A more powerful tool is found in computational fluid dynamics (CFD), which yields a more consistent and physically realistic flow field around a wind turbine than BEM and LL (see for example [6, 7, 8]). The main CFD approach utilised by the wind industry relies on the Reynolds Averaged Navier-Stokes (RANS) equations, which are a time-averaged version of the exact Navier-Stokes equations. Finally, another alternative is represented by Boundary Element Methods, also known as Panel methods, which have been developed for decades to perform calculation of incompressible potential flow of propellers and lifting-bodies.

The purpose of this work is the aerodynamic study under steady and unsteady inflow conditions of a wind turbine designed for the New MEXICO experiment using the three-dimensional panel method developed at Instituto Superior Técnico (IST), *PROPAN* [9]. The results obtained by *PROPAN* are compared with the New MEXICO data under steady and dynamic inflow conditions at specific wind and rotational speeds, in order to assess the current potentiality of the panel method in terms of steady and dynamic load forecasts and lay the foundations for further improvements and developments.

2. Mathematical formulation

2.1. Potential flow problem

Let us consider the rotor of a horizontal axis wind turbine with radius R and K blades symmetrically placed around the rotational axis, rotating with constant angular velocity Ω in an incompressible fluid extending to infinity in all directions. We introduce an inertial earth-fixed Cartesian coordinate system (x_0, y_0, z_0) and a Cartesian coordinate system (x, y, z) rotating with the turbine rotor, as shown in Figure 1. The x and x_0 axes coincide

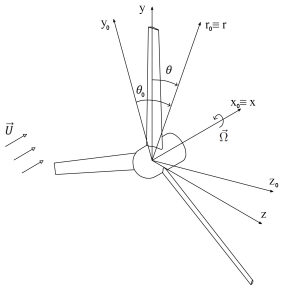

Figure 1: Coordinate system of the turbine.

with the turbine rotation axis, y_0 and z_0 are at the turbine plane, with y_0 pointing upwards. The y axis is coincident with the turbine reference line, passing through the reference point at the root section of the $k = 1$ blade, which represents the key blade, and z completes the right-hand system. It is worth adding the cylindrical coordinate systems (x_0, r_0, θ_0) and (x, r, θ), with

$$y_0 = r_0 \cos\theta_0, \;\; z_0 = r_0 \sin\theta_0, \;\; y = r\cos\theta, \;\; z = r\sin\theta \tag{1}$$

The relation between the two coordinate systems for a rotating right-handed rotor is

$$x_0 = x, \;\; r_0 = r, \;\; \theta_0 = \theta - \Omega t \tag{2}$$

where $\Omega = |\vec{\Omega}|$ and t is the time variable. The key blade reference line coincides with the y_0 axis at $t = 0$.

In the Cartesian reference system (x_0, y_0, z_0) the inflow is assumed to be steady, with the velocity $\vec{U}(x_0, y_0, z_0)$, while in the reference frame rotating with the turbine, the relative velocity field is time dependent and defined as

$$\vec{V}_\infty(x, r, \theta, t) = \vec{U}(x, r, \theta - \Omega t) - \vec{\Omega} \times \vec{x} \tag{3}$$

with $\vec{x} = (x, y, z)$.

The fluid flow is assumed to be inviscid and incompressible. The flow field velocity $\vec{V}(x, y, z, t)$ can be described as

$$\vec{V}(x, y, z, t) = \vec{V}_\infty(x, y, z, t) + \nabla\phi(x, y, z, t) \tag{4}$$

where $\nabla\phi(x, y, z, t)$ represents the gradient of a scalar perturbation potential equivalent to the irrotational velocity perturbation $\vec{v}(x, y, z, t)$. The potential satisfies the Laplace equation $\nabla^2\phi(x, y, z, t) = 0$.

The boundary of domain can be divided into two surfaces $\mathcal{S}_\mathcal{B}$ and $\mathcal{S}_\mathcal{H}$, representing the blade and hub, respectively. The perturbation potential needs to satisfy the following boundary conditions:

$$\nabla\phi \to 0, \;\; \text{if} \;\; r \to \infty \;\; \text{and} \;\; x \neq +\infty \tag{5}$$

and a Neumann boundary condition

$$\frac{\partial\phi}{\partial n} \equiv \vec{n} \cdot \nabla\phi = -\vec{n} \cdot \vec{V}_\infty \;\; \text{on} \;\; \mathcal{S}_\mathcal{B} \;\; \text{and} \;\; \mathcal{S}_\mathcal{H} \tag{6}$$

where $\partial/\partial n$ denotes differentiation along the normal and $\vec{n}$ is the unit vector normal to the surface directed outward from the surfaces.

When considering circulation around the blades, vortex sheets are shed from the trailing edge of each blade. There are two boundary conditions applying on the wake surface $\mathcal{S}_\mathcal{W}$: the normal component of the fluid velocity is continuous and equal to the normal velocity of the sheet

$$\vec{V}_w \cdot \vec{n} = \vec{V}^+ \cdot \vec{n} = \vec{V}^- \cdot \vec{n} \;\; \text{on} \;\; \mathcal{S}_\mathcal{W}, \tag{7}$$

and the pressure is continuous across the vortex wake

$$p^+ = p^- \text{ on } \mathcal{S}_\mathcal{W}, \tag{8}$$

where $\vec{V}$ is the fluid velocity, $\vec{V}_w$ the velocity of the points on the wake surface $\mathcal{S}_\mathcal{W}$, p is the static pressure and the indices + and − denote the the upper side and lower side of the vortex sheet. The unit vector normal to the vortex sheet is defined pointing from the lower − to the upper + side of the sheet. In order to define uniquely the circulation around the blade, the following Kutta condition must be imposed at the blade trailing edge

$$|\nabla\phi| < \infty \tag{9}$$

2.2. Integral equation of a potential flow

Let us assume $\bar{\phi} = 0$ for the interior region to $\mathcal{S}_\mathcal{B}$ and $\mathcal{S}_\mathcal{H}$, with $\bar{\phi}$ denoting the potential in the interior region to $\mathcal{S} = \mathcal{S}_\mathcal{B} \cup \mathcal{S}_\mathcal{H}$. Applying Green's second identity, the perturbation potential at a point p on the body surface can be expressed as

$$2\pi\phi\left(p,t\right) - \iint\limits_{\mathcal{S}_\mathcal{B}\cup\mathcal{S}_\mathcal{H}} \left[G\left(p,q\right)\frac{\partial\phi}{\partial n_q} - \phi\left(q,t\right)\frac{\partial G}{\partial n_q}\right] dS = \iint\limits_{\mathcal{S}_\mathcal{W}} \Delta\phi\left(q,t\right)\frac{\partial G}{\partial n_q} dS \tag{10}$$

where $G(p,q) = -1/R(p,q)$, with $R(p,q)$ being the distance between the field point p and the point q on the boundary $\mathcal{S}$. Since $\partial\phi/\partial n_Q$ on the surfaces $\mathcal{S}_\mathcal{B}$ and $\mathcal{S}_\mathcal{H}$ is known from the Neumann boundary condition on the body surface (Equation (6)), the Equation (10) is a Fredholm integral equation of the second kind in the dipole distribution $\mu(q,t) = -\phi(q,t)$ on the surfaces $\mathcal{S}_\mathcal{B}$ and $\mathcal{S}_\mathcal{H}$. The Kutta condition, Equation (9), yields the additional relationship between the dipole strength in the $\Delta\phi\left(q,t\right)$ wake and the surface dipole strength at the blade trailing edge.

2.3. Wake boundary conditions

The two boundary conditions on the wake are expressed by Equation (7) and Equation (8). The former implies that the vortex sheet moves with the fluid. If $S_w(\vec{x},t)$ denotes the equation of the vortex sheet surface $\mathcal{S}_\mathcal{W}$, then

$$\frac{\partial S_w}{\partial t} + \vec{V}^+\cdot\nabla S_w = \frac{\partial S_w}{\partial t} + \vec{V}^-\cdot\nabla S_w = 0 \tag{11}$$

Outside of the vortex sheet the Bernoulli equation for incompressible potential flow is

$$\frac{\partial\phi}{\partial t} + \frac{p}{\rho} + \frac{1}{2}|\vec{V}|^2 = \frac{p_\infty}{\rho} + \frac{1}{2}|\vec{V}_\infty|^2 \tag{12}$$

where p_∞ is the pressure of the undisturbed inflow and ρ the fluid density. Applying consecutively the Bernoulli equation at a given point on each side of the vortex sheet and subtracting:

$$\frac{\Delta p}{\rho} = -\frac{\partial(\Delta\phi)}{\partial t} - \frac{1}{2}\left(\left|\vec{V}^+\right|^2 - \left|\vec{V}^-\right|^2\right) \tag{13}$$

where $\Delta p = p^+ - p^-$ and $\Delta\phi = \phi^+ - \phi^-$ are the pressure and potential jumps across the sheet, respectively. From the boundary condition, Equation (8), the pressure-jump is zero, thus

$$\frac{\partial(\Delta\phi)}{\partial t} = -\frac{1}{2}\left(\left|\vec{V}^+\right|^2 - \left|\vec{V}^-\right|^2\right) \tag{14}$$

and knowing that

$$\left|\vec{V}^+\right|^2 - \left|\vec{V}^-\right|^2 = \left(\vec{V}^+ + \vec{V}^-\right)\cdot\left(\vec{V}^+ - \vec{V}^-\right), \tag{15}$$

it is possible to simplify Equation (12) as

$$\frac{\partial(\Delta\phi)}{\partial t} + \vec{V}_m\cdot\Delta\vec{V} = 0 \tag{16}$$

where $\vec{V}_m = \frac{1}{2}(\vec{V}^+ + \vec{V}^-)$ denotes the mean velocity and $\Delta\vec{V} = \vec{V}^+ - \vec{V}^-$ represents the velocity discontinuity on the wake surface. Using Equation (7), the velocity discontinuity may be written as the surface gradient of the potential discontinuity,

$$\frac{\partial(\Delta\phi)}{\partial t} + \vec{V}_m\cdot\nabla_S(\Delta\phi) = 0 \tag{17}$$

where $\nabla_S = -\vec{n}\times(\vec{n}\times\nabla)$ denotes the surface gradient. Equation (17) shows that the potential-jump remains constant following a fluid particle moving on the wake with the velocity $\vec{V}_m$.

In the general case, the instantaneous location of the wake has to be derived from Equation (11) and the dipole strength from Equation (17), which requires following the motion of the vortex sheet S_W in the unsteady flow velocity field. In this work a considerable simplification is introduced assuming a constant V_m equal to the undisturbed time averaged axisymmetric inflow. In the cylindrical coordinate system (x,r,θ),

$$\vec{V}_m = \left(\bar{U}(r), 0, \Omega r\right) \tag{18}$$

where $\bar{U}(r)$ is the zero harmonic of the axial inflow at the given radius, and Equation (17) becomes

$$\frac{\partial(\Delta\phi)}{\partial t} + \Omega\frac{\partial(\Delta\phi)}{\partial\theta} = 0 \tag{19}$$

The solution of Equation (19) is of the form $\Delta\phi(r,\theta,t) = \Delta\phi(r,t^*)$ with $t^* = t^*(\theta,t)$ being a characteristic convection time. If we consider $\theta = \theta_{te}$ at $t = 0$, where te stands for "trailing edge", we obtain

$$\Delta\phi(r,\theta,t) = \Delta\phi\left(r, t - \frac{\theta-\theta_{te}}{\Omega}\right) \tag{20}$$

Only the tangential induced velocity is neglected in the convection of vortices. The initial condition in the wake is

$$\Delta\phi(r,\theta,0) = \Delta\phi_{te}(r,0) = -\Gamma(r,0) \tag{21}$$

with Γ being the flow circulation for a circuit around the blade intersecting the wake at the blade trailing edge.

It is necessary to clarify that Equation (18) implies that the wake is aligned to the mean flow velocity field, which is not the actual case of this work where an empirical rigid wake is considered. However, Equation (19) is still used to compute the wake dipole strength.

2.4. Calculation of Velocity, Pressure and Forces
From the potential solution on the surface the covariant surface velocity components are calculated by means of a second order differentiation scheme of the potential relative to the arc lengths on the body surface grid. The pressure on the surface is obtained from the Bernoulli Equation (12). The pressure coefficient can be defined as

$$C_p = \frac{p - p_\infty}{1/2\rho V_\infty^2}, \tag{22}$$

with $V_\infty = |\vec{V}_\infty|$. The components of the inviscid force acting on the blades are obtained by integration of the pressure distribution on the blade surface.

3. Panel method

3.1. Integral equation discretisation
The numerical solution of the integral equation (10) is obtained using a low-order panel method in the time domain at the time steps $n = t/\Delta t$, where Δt is the constant time step. The body surfaces $\mathcal{S}_\mathcal{B} \cup \mathcal{S}_\mathcal{H}$ and the wake surface $\mathcal{S}_\mathcal{W}$ are discretised in quadrilateral panels having a hyperboloidal-shaped surface. The integrals over $\mathcal{S}_\mathcal{B}$ and $\mathcal{S}_\mathcal{H}$ are approximated by the summation of the integrals on the panels discretising the surfaces, assuming a constant strength of the dipole and source distributions on each panel. On the wake surface $\mathcal{S}_\mathcal{W}$ piecewise linear or constant dipole distributions are assumed, depending on the specific location of the panel.

Let $\mu_j^k(n) = -\phi_j^k(n)$ be the values at time step n of the dipole strength of the panel S_j^k on the surface of the k^{th} blade-hub sector, with $k = 1,\ldots,K$, $j = 1,\ldots,N$, and N being the number of panels on each blade-hub sector; let $\mu_{ml}^k(n) = -\Delta\phi_{ml}^k(n)$ be the values at time step n of the dipole strengths of the boundary between the panel $S_{m,l-1}^k$ and the panel S_{ml}^k of the k^{th} wake sector, with $m = 1,\ldots,N_R$, $l = 1,\ldots,N_W$, N_R being the number of panels along the spanwise direction and N_W the number of panels along the streamwise direction of the wake; let $\sigma_j^k(n)$ be the source strength of the panel S_j^k on the surface of the k^{th} blade-hub sector. If, at each time step n, Equation (10) is satisfied on the centre points P_i, $i = 1,\ldots,N_P$ of the $N_P = N \times K$ panels on the surface of the K blade-hub sectors, the so-called collocation points, it is possible to obtain a system of algebraic equations in the form

$$\sum_{k=1}^{K}\sum_{j=1}^{N}\left(\delta_{ij} - D_{ij}^k\right)\phi_j^k(n) - \sum_{k=1}^{K}\sum_{m=1}^{N_R}\sum_{l=1}^{N_W} W_{iml}^k \Delta\phi_{ml}^k(n) = \sum_{k=1}^{K}\sum_{j=1}^{N} S_{ij}^k \sigma_j^k(n), \quad i = 1,\ldots,N_P, \tag{23}$$

in which δ_{ij} is the Kronecker delta, D_{ij}^k and S_{ij}^k are the influence coefficients and W_{iml}^k is a wake influence coefficient which may be written as a linear combination of elementary integrals of the dipole type. This coefficients are calculated analytically following the formulation of Morino and Kuo [10]. The source strength $\sigma_k^k(n)$ is determined from the boundary condition, Equation (6), as

$$\sigma_k^k(n) = -\vec{n}_j^k \cdot \vec{V}_\infty(r_j^k, \theta_j^k, n\Delta t) \tag{24}$$

with $\vec{n}_j^k$ denotes the unit vector at the control point $(x_j^k, r_j^k, \theta_j^k)$ of the k^{th} blade. In order to reduce the dimension of the system of equations, the boundary condition is only applied at the key blade $k = 1$, therefore the contributions of the other blades are assumed to be known when solving for the key blade.

In the general case of a non-uniform axial inflow field, the solution in the rotating frame is periodic in time with a period, in general, equal to the time of a turbine revolution. We introduce the angular time step $\Delta\theta = \Omega\Delta t$. The total number of time steps is $N_t = N_{rev} \times N_\theta$, where N_{rev} is the number of revolutions for the time integration and $N_\theta = 2\pi/\Delta\theta$ is the total number of angular steps per revolution.

3.2. Calculation of Forces
The axial force T and the torque Q on the rotor are obtained by integration of the pressure distribution on the blade surfaces. Let (n_x, n_y, n_z) be the Cartesian components of the outward unit normal $\vec{n}$. The Thrust T can be expressed as

$$T = \iint_{S_B} p n_x dS, \tag{25}$$

and the Torque Q as

$$Q = \iint_{S_B} p\left(n_y z - n_z y\right) dS. \tag{26}$$

3.3. Wake models

In this thesis two wake models are utilised, a rigid wake and an aligned wake. The former is characterised by a fixed geometry where the vortex lines are empirically prescribed, while the latter comprehends an iterative alignment based on the pitch modification on the wake vortices. For both models, the contraction or expansion of the wake geometry is not allowed.

In the rigid model the wake generation is based upon empirical knowledge which allows to specify the geometry of the wake surface. The dipole strength at the wake surface can be related to the potential discontinuity at the blade trailing edge by the application of the so-called Morino Kutta condition [10], written in the form

$$\Delta\phi = \phi^+ - \phi^-, \tag{27}$$

in which ϕ^+ and ϕ^- are the values of the potentials at the trailing edge, respectively on the upper and lower sides of the blade.

In the wake alignment model the corner points of the blade wake grid panels are displaced with the mean fluid velocity. At the $(h+1)^{\text{th}}$ iteration, the geometry in cylindrical coordinates of the wake strip $i+1$ can be determined by using an Euler scheme [11]:

$$\begin{aligned} x_{i+1}^{(h+1)} &= x_i^{(h)} + V_x\left(x_i^{(h)}, r_i^{(h)}, \theta_i^{(h)}\right)\Delta t, \\ r_{i+1}^{(h+1)} &= r_i^{(h)} + V_r\left(x_i^{(h)}, r_i^{(h)}, \theta_i^{(h)}\right)\Delta t, \\ \theta_{i+1}^{(h+1)} &= \theta_i^{(h)} + \frac{V_\theta\left(x_i^{(h)}, r_i^{(h)}, \theta_i^{(h)}\right)\Delta t}{r_i^{(h)}}, \end{aligned} \tag{28}$$

where V_x, V_r and V_θ are the components of the mean vortex sheet velocity along the axial, radial, and circumferential directions, respectively, and Δt is the time step for the Euler vortex convection scheme. The velocity components are calculated from the integral equation of the velocity, derived from Equation (23).

3.4. Viscous effects

In order to consider the viscous effects, it is possible to apply quasi-steady corrections to the inviscid axial force and power calculated with the panel method [12]. Figure 2 shows the velocity triangle. The viscous forces on the turbine blades are calculated using the concept of section lift and drag force that can be derived from two-dimensional lift and drag data. In particular, the inflow angle β_i is linked to the inviscid thrust T_i and torque Q_i by the relation

$$\tan\beta_i = \frac{dQ_i}{r dT_i} \tag{29}$$

and the angle of attack can be derived as $\alpha = \beta_i - \psi$, where ψ is the pitch angle. The angle of attack is key to extract experimental data of the lift and drag coefficient, C_L and C_D respectively.

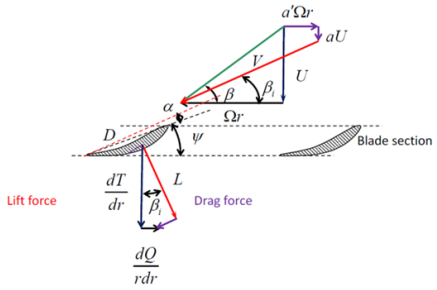

Figure 2: Blade velocity triangle [13].

The viscous thrust T_v and torque Q_v are then expressed as

$$dT_v = (L_v\cos\beta_i + D\sin\beta_i)dr, \tag{30}$$
$$dQ_v = (L_v\sin\beta_i - D\cos\beta_i)dr \tag{31}$$

where the viscous lift L_v is given as

$$L_v = L_i\frac{C_{L_v}}{C_{L_i}} \tag{32}$$

and the drag D as

$$D = \frac{1}{2}\rho C_D V^2 c \tag{33}$$

In Equation (33), the velocity V can be calculated by the Kutta-Joukowski law in steady flow:

$$L_i = \rho V\Gamma \tag{34}$$

In this work, the correction on the lift force (Equation (32)) is neglected for simplicity, thus the viscous thrust and torque (Equation (30) and (31)) become

$$dT_v = (L_i\cos\beta_i + D\sin\beta_i)dr, \tag{35}$$
$$dQ_v = (L_i\sin\beta_i - D\cos\beta_i)dr \tag{36}$$

4. Results

4.1. Steady inflow

A detailed numerical study has been performed with wind velocities of 10.05 m/s ($TSR = 10$) and 15.06 m/s ($TSR = 6.7$) using the wake alignment model, in order to define the best blade, hub and wake grids in terms of grid plot convergence, smoothness of wake geometry (surface) and viscous C_P and C_T. The parameters subject to this study are wake length (x_W), radial (N_R) and chordwise (N_C) number of panels along the blade, upstream (N_{hu}) and downstream (N_{hd}) number of panels on the hub. More in detail, the tests are performed with $x_W = [4R, 6R, 8R, 10R, 12R, 14R]$, $N_R = [30, 40, 50, 60, 70, 80]$, $N_C = [60, 70, 80, 90, 100]$,

$N_{hu} = [30, 35, 40]$ and $N_{hd} = [45, 55, 65]$. To evaluate the convergence of the results, three quantities have been analysed: the pressure distributions at $25\%, 35\%, 60\%, 82\%$ and 92% radial positions, the dimensionless circulation ($\frac{\Gamma}{\Omega R^2}$), the viscous power and thrust coefficients C_P and C_T.

The optimal parameters resulted from this study are shown in Table 1.

	x_W	N_R	N_C	N_{hu}	N_{hd}
$TSR = 6.7$	12R	80	80	30	45
$TSR = 10$	12R	80	90	30	45

Table 1: Numerical optimal grid parameters at $TSR = 6.7$ and $TSR = 10$.

The calculated (*Sim*) and measured (*Exp*) pressure profiles at $TSR = 6.7$ and $TSR = 10$ for some radial positions are presented in Figure 3 and Figure 4, respectively. Clearly, the simulated pressure

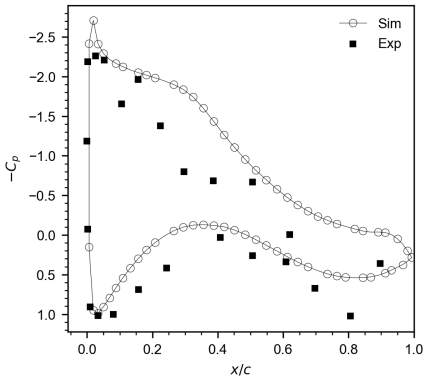

(a) $r/R = 25\%$

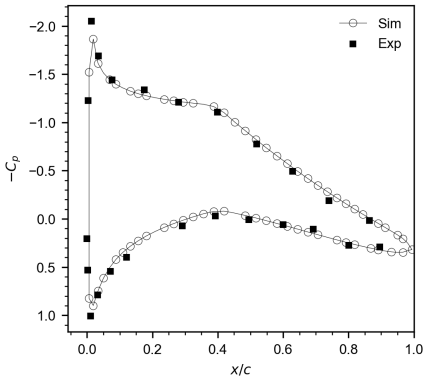

(b) $r/R = 92\%$

Figure 3: Numerical pressure coefficient comparison with experimental results at $TSR = 6.7$.

distribution matches outstandingly the experimental measurements at $r/R = 92\%$. Indeed, the only visible discrepancies are a greater suction peak pressure at the leading edge (at $TSR = 6.7$) and a slight underestimation along the pressure side of the blade sections (at $TSR = 10$). On the other hand, the same precision is not found for the remaining radial positions.

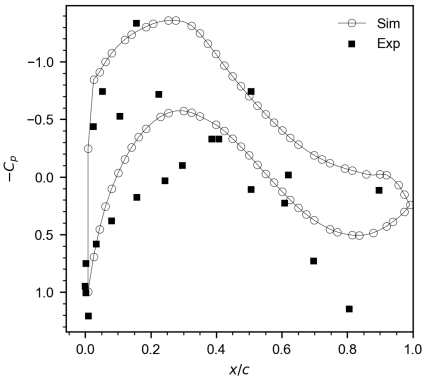

(a) $r/R = 25\%$

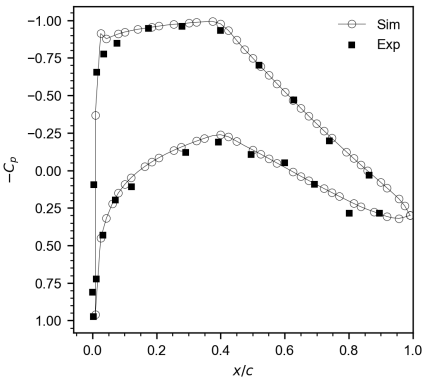

(b) $r/R = 92\%$

Figure 4: Numerical pressure coefficient comparison with experimental results at $TSR = 10$.

The largest mismatch can be seen for the pressure profiles at $r/R = 25\%$. For both TSRs the predicted pressure is smaller on the suction and pressure sides along the central region of the blade section. One possible reason is that the blade wake is truncated and does not connect with the hub surface. Therefore, in the cylindrical part, no vorticity is shed from the trailing edge. Overall, it is worth noting that for $r/R = 25\%$ the experimental data do not have reasonable values for some chordwise locations, especially where the pressure coefficient is greater than 1, meaning that some sensors recorded wrong measurements (e.g at $x/c = 0.8$). Finally, the pressure distributions obtained with *PROPAN* are qualitatively coherent with the ones outputted by the CFD codes participating in the New MEXICO project. Indeed, as concluded in the final New MEXICO report [14] the experimental resolution of the pressure sensors is insufficient, especially at the lower inflow speeds, resulting in non-smooth mea-

sured pressure plots.

Table 2 and Table 3 show the comparison of the power and thrust coefficients between the simulated results and the experimental data. A very small relative difference is recorded for the power coefficient (ΔC_P) - less than 1% - for both TSRs, while the estimate of C_T is far less precise. Indeed, although a reasonably small ΔC_T at $TSR = 10$, the thrust on the blades is overestimated by more than 9% at $TSR = 6.7$. The main probable cause of this behaviour lies in the underestimation of the pressure levels at the suction side of the inner parts of the blades, as described in the previous section, which leads to higher load predictions. More in detail, this trend is more pronounced on the pressure profiles at $TSR = 6.7$, which justifies the lower precision for this case.

	$\boldsymbol{C_P}$	$\boldsymbol{C_T}$	$\lvert\boldsymbol{\Delta C_P}\rvert$[%]	$\lvert\boldsymbol{\Delta C_T}\rvert$[%]
Exp	0.4358	0.7742	-	-
Sim	0.4397	0.8458	0.9061	9.243

Table 2: Power and thrust coefficients comparison between simulated and experimental results at $TSR = 6.7$.

	$\boldsymbol{C_P}$	$\boldsymbol{C_T}$	$\lvert\boldsymbol{\Delta C_P}\rvert$[%]	$\lvert\boldsymbol{\Delta C_T}\rvert$[%]
Exp	0.3153	1.019	-	-
Sim	0.3166	1.041	0.4131	2.234

Table 3: Power and thrust coefficients comparison between simulated and experimental results at $TSR = 10$.

4.2. Dynamic inflow

The study of the dynamic inflow conditions focusses on a specific New MEXICO experimental set-up. This is because wind velocity, rotational speed and consequently TSR are almost identical to the axial flow steady case with $TSR = 10$, allowing to utilise the best grid geometry yielded by the steady inflow numerical study. More specifically, the dynamic behaviour of the wind inflow is caused by a variation of the blade pitch angle, which changes from $-2.3°$ to $5.0°$ and eventually back to $-2.3°$, thus it is possible to define three different stages throughout the duration of the experiment, which is about 15 seconds. In Figure 5 the experimental trend of the blade pitch angle ψ is illustrated as an example to visualise the distinction of the three stages. The first stage is coincident with the axial flow steady case, thus the results achieved from the optimal numerical grid of the steady flow numerical tests are considered constant for the whole timespan of this stage. For the second and third stage, two different geometries have been defined based on the aligned

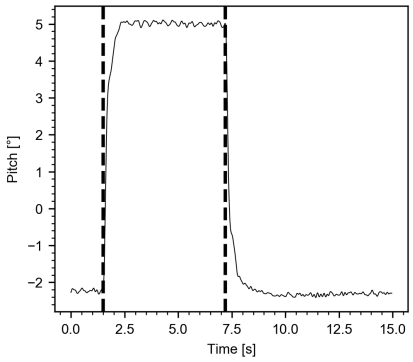

Figure 5: Stages definition - the different stages are separated by the dashed vertical lines.

wake model and the rigid wake model outlined previously (with the rigid wake model being used for the unsteady calculations). The first method, arbitrarily denominated *IAW* (Independent Aligned Wake), consists of performing three steps:

1. Create a simple wake geometry modifying the pitch distribution at the blade trailing edge accordingly to the stage pitch variation,

2. Run a steady simulation activating the wake alignment model for each stage of the dynamic inflow test,

3. Utilise the aligned wake outputted from the simulation as the rigid wake input geometry for the dynamic simulation.

The strength of this approach is to obtain an aligned wake geometry consistent to the pitch variation, while its weakness is to provoke an abrupt transition between the stages. Indeed, the perturbation caused by the pitch modification does not propagate with the same velocity over the wake, meaning that the wake needs more time to adjust to the new blade pitch configuration. Eventually, two distinct aligned wake geometries have been created with this method, one with respect to a blade pitch equal to $-2.3°$ (for Stage 1 and 3) and the other one to $\psi = 5.0°$ (for Stage 2).

The second method, denominated *EAW* (Empirical Aligned Wake), rely on the wake geometry utilised for Stage 1, therefore aligned to the incoming wind flow with $\psi = -2.3°$. It comprehends the following actions:

1. Extract the wake radial pitch distributions at some determined axial (streamwise) positions from the previous stage,

2. Create a rigid wake geometry modifying the pitch distribution at the blade trailing edge ac-

cordingly to the stage pitch variation and specifying the quantities highlighted in point 1.

In this case the wake geometry is highly dependent on the flow conditions occurring before the pitch variation, since the wake is forced to be consistent to the previous one except at the trailing edge. This might help to better predict the behaviour in the transition periods but lacks of accuracy due to the non-alignment of the wake in relation to the local flow. For every stage, the axial positions (in dimensionless form) selected to extract the wake properties are $x/R = [0.05, 0.10, 0.25, 0.50, 1.0]$.

The inviscid normal and tangential force coefficients $C_n = \frac{F_n}{1/2\rho V_\infty^2 c}$ and $C_t = \frac{F_t}{1/2\rho V_\infty^2 c}$ obtained from the simulations are compared to the experimental ones, Figure 6 and Figure 7. It is worth mentioning that due to the large recorded oscillations, the measured data has been denoised through the application of a moving average function.

Starting from analysing Stage 1 (in which the numerical steady-flow wake geometry is used), a good prediction of the results is calculated only for the C_n at $r/R = 92\%$. For the remaining blade sections, the simulated C_n and C_t are consistently different from the experimental data, especially towards the blade root.

When the pitch is varied to the Stage 2 configuration, the experiments show a clear undershoot in the forces, which presents some oscillations leading to a "double" negative peak. The same observation can be drawn from the transient phase between Stage 2 and Stage 3: there is a distinct overshoot with two positive peaks before stabilising to the equilibrium. This phenomenon do not happen in reality, therefore it is believed to be due to a fault in the pressure sensors, which might be affected by the tower vibrations.

In Stage 2, the overall trends of the simulated force coefficients are qualitatively consistent to the experimental measurements, even though large discrepancies occur in the transient time frame, where unexpected peaks are seen. In particular, the trend of the simulated normal force coefficients is similar to the experimental one, except for the radial positions closer to the blade root where the *EAW* method largely underestimates the forces at the equilibrium. The *IAW* geometry yields the best outcomes in terms of agreement with the experimental results for every radial position but $r/R = 60\%$, where the normal forces are slightly overestimated.

The opposite tendency is observed for the tangential force coefficients: the *EAW* results are always closer to the experimental data than the *IAW* ones.

Regarding Stage 3, clearly the predicted overshoot is extremely overestimated for both C_n and

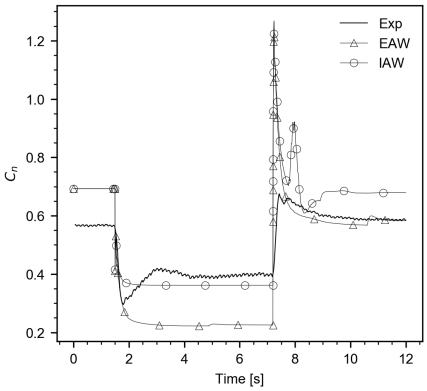

(a) $r/R = 25\%$

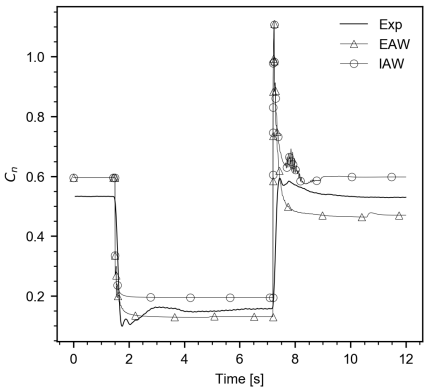

(b) $r/R = 60\%$

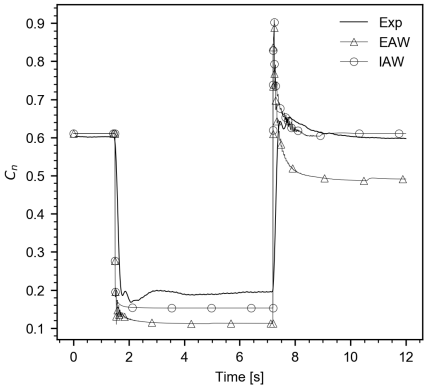

(c) $r/R = 92\%$

Figure 6: All stages normal forces coefficient comparison between experimental, *IAW* and *EAW* results for different radial positions.

C_t. The results obtained for the normal force coefficients suggest that, compared to Stage 2 where the *IAW* geometry is the most accurate for every radial position but one, the *EAW* method predicts C_n at $r/R = 25\%$ with great precision and differs from the experimental data with the same magnitude of the *EAW* method at $r/R = 60\%$. For the remaining radial positions, the *IAW* geometry yields the best

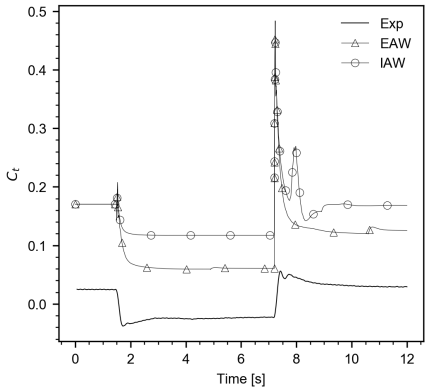

(a) $r/R = 25\%$

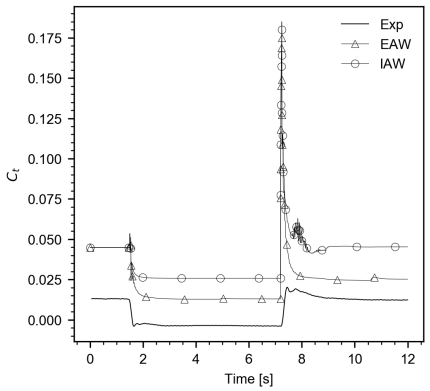

(b) $r/R = 60\%$

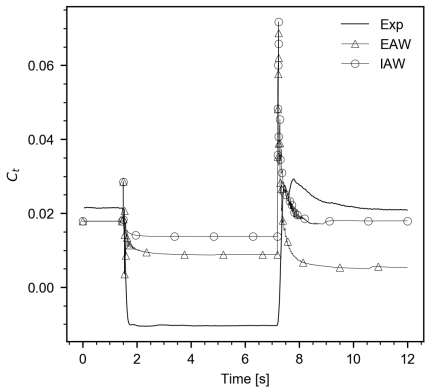

(c) $r/R = 92\%$

Figure 7: All stages tangential forces coefficient comparison between experimental, *IAW* and *EAW* results for different radial positions.

outcomes, especially at $r/R = 92\%$. On the other hand, the *EAW* estimates are more precise for the tangential forces, performing better than the *IAW* geometry for three radial positions. In addition, it can be seen that the *EAW* steady results are different from the Stage 1 results, indicating that the initial and final wake geometries are not coincident.

Finally, the following main considerations can be outlined:

- On the whole, the panel method predictions are in reasonable agreement with the experimental measurements, particularly when reaching the steady solution, making the panel method a reliable tool.

- From the comparison of the normal and tangential forces along the blades, no specific wake method is clearly the optimal one. The *IAW* geometry has a greater accuracy than the *EAW* one on the normal forces coefficient, while the opposite trend is observed for the tangential forces. However the *EAW* geometry is more unstable in terms of numerical oscillations.

- Compared to the steady calculations, the time required for running the dynamic simulations (utilising one CPU) is considerably larger. For instance, the computational time of the results obtained for Stage 2 is around 140 hours, equal to about 6 days, on a Xeon processor at 2.6GHz with 125GB of RAM. If one takes into account the duration of all the stages, then an average of 3.5 hours per rotor revolution can be assessed.

- The main discrepancies between the simulated and experimental results are seen in the transient time frames, especially in the one between the second and third stage.

5. Conclusions

A thorough numerical study under steady inflow conditions has been described, aiming at assessing the best wake geometry and grid configuration for two undisturbed wind velocities, 10.05 m/s ($TSR = 10$) and 15.06 m/s ($TSR = 6.7$). A wake alignment model was used for all the tests. Convergence of the numerical results is achieved with a longer wake length and greater grid refinement along the radial and chordwise direction of the blade, while no relevant differences are observed for the hub. When comparing the simulated results with the experimental data, a good agreement is generally found. The predictions of the pressure distribution are extremely accurate for the sections closer to the blade tip, while small discrepancies are seen towards the root. Power coefficients also match precisely the experimental data for both TSRs, having a relative error of less than 1%. However, the same accuracy can not be reached for the thrust coefficients, with the largest relative error (about 10%) happening at $TSR = 6.7$.

When passing to the dynamic simulations, the numerical optimal grid obtained at $TSR = 10$ was utilised, since only one dynamic case from the New

MEXICO measurements was considered for validation purposes. The dynamic variation of the blade pitch angle ψ has been simulated through the definition of three different stages, assuming an instantaneous behaviour. The first stage represents the steady inflow condition studied in the numerical tests. For the second and third stage, two different methods to create the wake geometry were applied, with the main difference of yielding a wake geometry partially or fully aligned to the incoming wind flow. The experimental normal and tangential forces experienced on blade at five specific sections were compared to the simulated results. Overall, the trends of the forces predicted with both wake geometries are comparable to the experimental ones when achieving the periodic solution. However, the main limitation of *PROPAN* lies in the inaccurate estimation of the force undershoot and overshoot occurring in the first instances of Stage 2 and 3, respectively. Additionally, high-frequency numerical oscillations are witnessed, suggesting that further analyses on the geometry and grid quality of the turbine model must be done.

Acknowledgements

The author would like to thank his supervisors Dr. João Baltazar and Prof. Ricardo Pereira who have given him the opportunity to work on a thesis related to a field he has always been interested about, wind energy. In particular, he would like to express his gratitude to Dr. João Baltazar for his constant support and guidance throughout the realisation of this thesis.

References

[1] S. Sang, Hao Wen, A.X. Cao, X.R. Du, X. Zhu, Q. Shi, and C.H. Qiu. Dynamic modification method for BEM of wind turbine considering the joint action of installation angle and structural pendulum motion. *Ocean Engineering*, 215:107528, 2020.

[2] J G Schepers. IEA Annex XX. Dynamic Inflow effects at fast pitching steps on a wind turbine placed in the NASA-Ames wind tunnel, Oct 2007.

[3] Jan Gerhard Schepers. *Engineering models in wind energy aerodynamics: Development, implementation and analysis using dedicated aerodynamic measurements*. PhD thesis, TU Delft, 2012.

[4] S Hauptmann, M Bülk, L Schön, S Erbslöh, K Boorsma, F Grasso, M Kühn, and P W Cheng. Comparison of the lifting-line free vortex wake method and the blade-element-momentum theory regarding the simulated loads of multi-MW wind turbines. *Journal of Physics: Conference Series*, 555:012050, dec 2014.

[5] Brenden Epps and Richard Kimball. Unified Rotor Lifting Line Theory. *Journal of Ship Research*, 57:181–201, 12 2013.

[6] N Sørensen and M Hansen. Rotor performance predictions using a Navier-Stokes method. In *1998 ASME Wind Energy Symposium*, page 25, 1998.

[7] Guanpeng Xu and Lakshmi N Sankar. Computational study of horizontal axis wind turbines. *J. Sol. Energy Eng.*, 122(1):35–39, 2000.

[8] N Sørensen and Jess Michelsen. Aerodynamic predictions for the unsteady aerodynamics experiment phase-II rotor at the National Renewable Energy Laboratory. In *2000 ASME Wind Energy Symposium*, page 37, 2000.

[9] João Baltazar. *On the Modelling of the Potential Flow About Wings and Marine Propellers Using a Boundary Element Method*. PhD thesis, IST, 2008.

[10] Luigi Morino and Ching-Chiang Kuo. Subsonic Potential Aerodynamics for Complex Configurations : A General Theory. *AIAA Journal*, 12(2):191–197, 1974.

[11] J Baltazar, J A C Falcão de Campos, and J Bosschers. Open-Water Thrust and Torque Predictions of a Ducted Propeller System with a Panel Method. *International Journal of Rotating Machinery*, 2012.

[12] J. Baltazar and J A C Falcão de Campos. Unsteady Analysis of a Horizontal Axis Marine Current Turbine in Yawed Inflow Conditions With a Panel Method. 06 2009.

[13] Ricardo Santos Pereira. Lecture Slides - The Blade Element Momentum Theory of a Turbine.

[14] K Boorsma, J G Schepers, S Gomez-Iradi, I Herraez, T Lutz, P Weihing, L Oggiano, G Pirrung, H A Madsen, W Z Shen, H Rahimi, and P Schaffarcyk. Final report of IEA Wind Task 29 Mexnext (Phase 3). Technical report, ECN, 2018.